MATERIALS SCIENCE

Ultrahigh sensitive Raman spectroscopy for subnanoscience: Direct observation of tin oxide clusters

Akiyoshi Kuzume[1]*, Miyu Ozawa[2], Yuansen Tang[2], Yuki Yamada[2], Naoki Haruta[1†], Kimihisa Yamamoto[1,2]*

Subnanometric metal clusters exhibit anomalous catalytic activity, suggesting innovative applications as next-generation materials, although identifying and characterizing these subnanomaterials in atomic detail remains a substantial challenge because of the severely weak signal intensity for the conventional analytical methods. Here, we report a subnanosensitive vibrational technique established based on the surface-enhanced Raman spectroscopy, demonstrating the first-ever detailed vibrational characterization of subnanomaterials. Furthermore, combining with density functional theory calculations, we reveal that inherent surface structures of the tin oxide subnanoclusters determine the size-specific spectral and catalytic characteristics of these clusters. The high-sensitivity characterization methodology elaborated here can provide a comprehensive understanding of the chemical and structural natures of subnanomaterials, which facilitate the rational design of subnanomaterials on the atomic scale for practical applications, such as in catalysts, biosensors, and electronics.

INTRODUCTION

Metal nanoparticles are one of the most widely used materials in innovative research and development studies within a variety of fields and have numerous potential applications, such as in antibiotics, optics, plasmonics, catalysts, and electronics. There have also been many studies aimed at the production of homogeneous nanocrystals, which exhibit narrow size and shape distributions, so as to determine the effect of size on the chemical and physical properties of these materials. Recently, there has been a breakthrough in the fabrication of monodisperse nanocrystals in the size range of 0.5 to 2.0 nm in diameter. These so-called subnanoclusters (SNCs) (*1*) can now be obtained via wet processes that are readily scalable for further application researches. The precise preparation of SNCs is realized using nanosynthesizers, such as dendritic phenylazomethine derivatives (*2*, *3*), in which a precise number of metal complexes is first accumulated at the imine parts within the dendrimer molecules. Subsequently, multinuclear complexed molecules were chemically reduced to form size-monodispersed metal clusters within the template molecule. This approach is extremely general and widely applicable to many of the metallic elements in the periodic table (*4*). SNCs exhibit distinctive discrete characteristics with the number of constituting atoms (atomicity), such as unexpectedly high catalytic activity on the electrochemical oxygen reduction reaction (*5*–*8*) and the aerobic oxidation of hydrocarbons (*9*–*11*), as well as a quantum size effect with notable shifts in bandgap energy (*12*). However, a detailed evaluation of physical and chemical properties of SNCs in literature is still in early stage.

The spectroscopic detection of subnanoscale materials, in general, is difficult because of a severely weak signal intensity that results from the small sizes of these materials, as well as the limited sensitivity and accuracy of conventional techniques. In addition, the surface coverage of SNCs on a support can be an issue. SNCs are not stable and will readily aggregate if they are not supported or if the surface coverage is overly high on a support. Thus, SNCs supported on carbon, silicate, graphene, and other substrates must be at a concentration as low as 0.4 weight % (wt %) to guarantee sufficient distance between neighboring clusters, so as to avoid surface agglomeration (*13*). As a consequence, the detection limit of conventional spectroscopic methods is far below the level required to detect isolated SNCs, and thus, it is extremely difficult to examine in detail the atomicity-dependent characteristics of subnanomaterials.

In the realm of nanoscience, one of the most intriguing materials is tin (Sn) oxide, which is both inexpensive and abundant. Intensive researches have therefore been conducted with regard to a wide range of applications, such as in gas sensors, catalysts, and transparent conductors (*14*–*16*). Recently, our group reported a correlation between the chemical composition and the catalytic activity of Sn oxide SNCs during the CO oxidation reaction (*17*). Size-controlled Sn oxide clusters with diameters between 0.9 and 1.6 nm were fabricated using a dendrimer template method. These materials showed a size-dependent composition variation such that the Sn^{2+} fraction increases with decreasing size, while the catalytic activity during CO oxidation increased with decreasing size. However, the correlation between the chemical composition and catalytic activity is hypothetical at present. Therefore, a detailed comprehensive understanding of the chemical and structural states of Sn oxide SNCs is essential.

Here, we report a highly sensitive analytical technique based on the principles of surface-enhanced Raman spectroscopy (SERS) aiming for the analysis of subnanoscale particles (Fig. 1). In this work, the spectral analyses of the unique Raman signals of Sn oxide SNCs are complemented by theoretical structural and vibrational analyses to clarify the origin of the Raman characteristics of SNCs. The resulting structural and chemical information further explain the specific size-dependent catalytic activity of Sn oxide SNCs during the CO oxidation reaction. This study demonstrates comprehensive understanding of the chemical and structural natures of subnanomaterials, which will facilitate the rational design of subnanomaterials such as catalysts.

RESULTS

Development of subnanosensitivity Raman spectroscopy

SERS is a powerful analytical technique capable of providing fingerprint information regarding target substances. The vibrational signals associated with SERS are greatly enhanced in the presence of Au or

[1]JST-ERATO, Yamamoto Atom Hybrid Project, Tokyo Institute of Technology, Yokohama 226-8503, Japan. [2]Laboratory for Chemistry and Life Science, Tokyo Institute of Technology, Yokohama 226-8503, Japan.
*Corresponding author. Email: yamamoto.k.at@m.titech.ac.jp (K.Y.); kuzume.a.aa@m.titech.ac.jp (A.K.)
†Present address: Fukui Institute for Fundamental Chemistry, Kyoto University, Kyoto 606-8103, Japan.

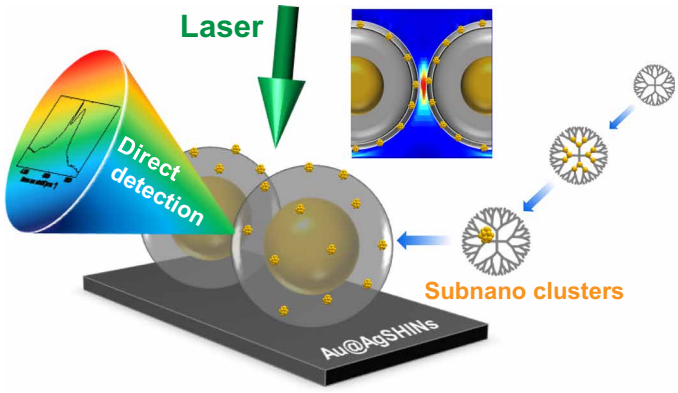

Fig. 1. A schematic diagram of the direct detection of SNCs. Tin oxide SNCs finely prepared by a dendrimer template method are loaded on the thin silica shell layers of plasmonic amplifiers such that the Raman signals of the SNCs are substantially enhanced to a detectable level. The strength of the electromagnetic fields generated due to the surface plasmon resonance properties of the Au or Ag nanoparticles decays exponentially with distance from the surface. Therefore, a rational interfacial design between the amplifiers and SNCs is the key to acquiring strong Raman signals.

Ag nanoparticles, which work as optical amplifiers. Shell-isolated nanoparticle enhanced Raman spectroscopy (SHINERS) (*18*) is an advanced SERS technique, which uses Au or Ag amplifiers coated with 2- to 3-nm-thick silica shells. The presence of these silica shells inhibits chemical and electrical interactions between target molecules and the optical amplifiers such that only the intrinsic characteristics of the target molecules are assessed. This configuration also allows using any type of substrates in terms of shapes and materials, providing extensive applicability of this technique to interfacial analyses. However, even the conventional SHINERS method, in which Au nanoparticles with a diameter of 55 nm are used, cannot "sense" the presence of SNCs under such a low surface density condition.

The sensitivity of SERS strongly depends on the spatial design of the hotspots generated at the gaps between neighboring shell-isolated nanoparticles (SHINs). It is at these gaps that specific surface plasmon resonance phenomena appear in response to laser irradiation, which, in turn, lead to pronounced enhancement of the Raman signals. Therefore, a key aspect of obtaining high-sensitivity Raman data is the successful design and fabrication of the plasmonic amplifiers. For this reason, the present work first performed a theoretical study to optimize the design of the plasmonic amplifiers.

A three-dimensional finite-difference time-domain (3D-FDTD) simulation was used to compute the electromagnetic field distribution and the enhancement characteristics of the hotspots, based on various materials and structural configurations (*19*). The enhancement properties of model gaps between two Ag core SHINs located on smooth Si surfaces were compared while varying the core size (Fig. 2A). These calculations showed that the maximum Raman scattering intensity was obtained for Ag core SHINs with a diameter of 100 nm.

On this basis, spherical, highly homogeneous, 100-nm-diameter Ag nanoparticles with a narrow size distribution were synthesized using a seed-mediated multistep process (Fig. 2B; see also details in Materials and Methods). In this process, Au core nanoparticles with diameters in the range of 45 ± 5 nm were prepared on the basis of the traditional Frens method, using sodium citrate (fig. S1A) (*20*). Subsequently, these nanoparticles were covered with thick Ag shells to obtain the desired 100 nm diameter, thus producing Au-core Ag-shell nanoparticles (Au@Ag NPs) (*21*). Note that the Au cores were introduced so as to increase both the stability and shape homogeneity of the Ag outer layers, while the size of the Au core less than 70 nm was found to have a negligible impact in terms of enhancement properties, as estimated by 3D-FDTD simulation with different Au core sizes (Fig. 2C). These Au@Ag NPs were further coated with silica shells using a solution containing both 3-aminopropyltriethoxysilane (APTES) and silicate at room temperature (*22*) to form Au@Ag SHINs (Fig. 2D). The silica shell layers on the surfaces of amplifiers had thicknesses in the range of 2 to 3 nm (fig. S2A) and provided a porous outer layer to which SNCs could adhere. Enhanced electromagnetic fields appear at the surfaces of these SHINs and decay exponentially with distance from the surfaces (fig. S2, B and C). Therefore, this spectroscopic technique selectively generates Raman signals of substances that are situated in close proximity to the surfaces of the SHINs.

The signal enhancement properties of Au@Ag SHINs with core sizes of 70 and 115 nm (fig. S1, B to G) were also evaluated to confirm the superiority of 100-nm SHINs, as suggested by the 3D-FDTD simulations (Fig. 2A). Raman enhancement ratios of eight and nine times were found for 70- and 115-nm Au@Ag SHINs, respectively, while 100-nm particles enhanced the signal by a factor of 33 (Fig. 2E). This notable quantitative agreement between simulated and experimental results substantiated the significant enhancement obtained from the current 100-nm Au@Ag SHINs. This phenomenon can be explained by the coupling effect between the absorption wavelength of the surface plasmon resonance from the Au@Ag NPs (fig. S1B) and the wavelength of the incident laser source (532 nm).

Analyses of Sn oxide SNCs using the SHINERS technique

Sn oxide SNCs were prepared by our original synthetic technique to allow direct spectroscopic observation (Fig. 3) using fourth-generation dendritic phenylazomethine with a tetraphenylmethane core (DPA-TPM-G4) (*23*, *24*) as a template molecule, which offers precise size control (*2*, *3*). In this technique, the potential gradient properties of dendrimer molecules induce the stepwise accumulation of metal complexes from the inner generation layers toward the outer generation layers during the titration of metal salts (fig. S3). Each respective layer consists of 4, 8, 16, and 32 imine sites, and a gradual multistep accumulation process allows the formation of stable monodispersed complexes containing 4, 12 (=4 + 8), 28 (=12 + 16), and 60 (=28 + 32) metal atoms, respectively (Fig. 3B) (*3*). After chemical reduction by $NaBH_4$, analysis by high-angle annular dark-field scanning transmission electron microscopy (HAADF-STEM) found that the sizes of the Sn_{12}, Sn_{28}, and Sn_{60} oxide SNCs were 0.9 ± 0.2 nm, 1.0 ± 0.2 nm, and 1.8 ± 0.3 nm, respectively (fig. S4). The sizes observed in these STEM images agree with the trends determined using atomic force microscopy (AFM) and demonstrate the obvious effect of the amount of $SnCl_2$ added to the DPA-PTM-G4 molecules (fig. S4, D to F).

The oxidation states of the Sn atoms in the SNCs were evaluated by Sn $3d_{5/2}$ core-level x-ray photoelectron spectroscopy (XPS). In each case, a significant contribution of a shoulder peak on the lower binding energy edge was apparent (fig. S5), indicating the formation of substoichiometric SnO_x ($1 < x < 2$) species intermediate between SnO and SnO_2. The proportion of Sn^{2+} in the materials in the present study was slightly higher than that obtained in a previous study in which Sn oxide SNCs were calcined at 600°C on mesoporous silica substrates (*17*). Therefore, the oxidation state of the Sn oxide SNCs

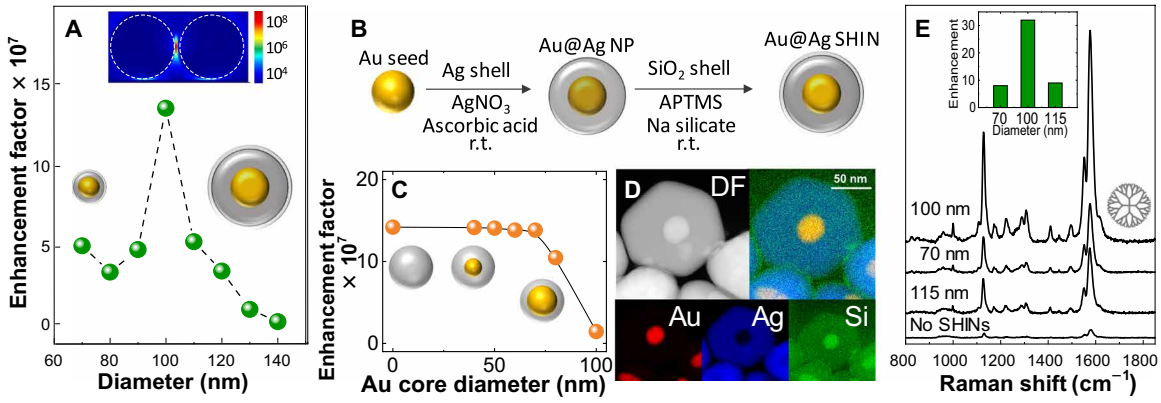

Fig. 2. Fabrication and characterization of Au@Ag SHINs as optical amplifiers. (**A**) A simulation of the maximum size-dependent enhancement at the hotspot between two shell-isolated Ag nanoparticles (Ag SHIN) as calculated by 3D-FDTD simulations (inset). (**B**) Schematic of the synthesis of Au@Ag SHINs. (**C**) Maximum enhancement factors calculated by 3D-FDTD simulation for 100-nm-diameter Au@AgSHINs with different Au core sizes. (**D**) HAADF-STEM image with corresponding EDS mapping images of Au@Ag SHINs. (**E**) A series of SHINER spectra of DPA-TPM-G4 acquired with Au@Ag SHINs having 70-, 100-, and 115-nm particle sizes, compared with a normal Raman spectrum acquired without SHINs as a reference. Inset: Raman enhancement ratios calculated by comparing the signal intensities in SHINER spectra and a standard normal Raman spectrum acquired without SHINs.

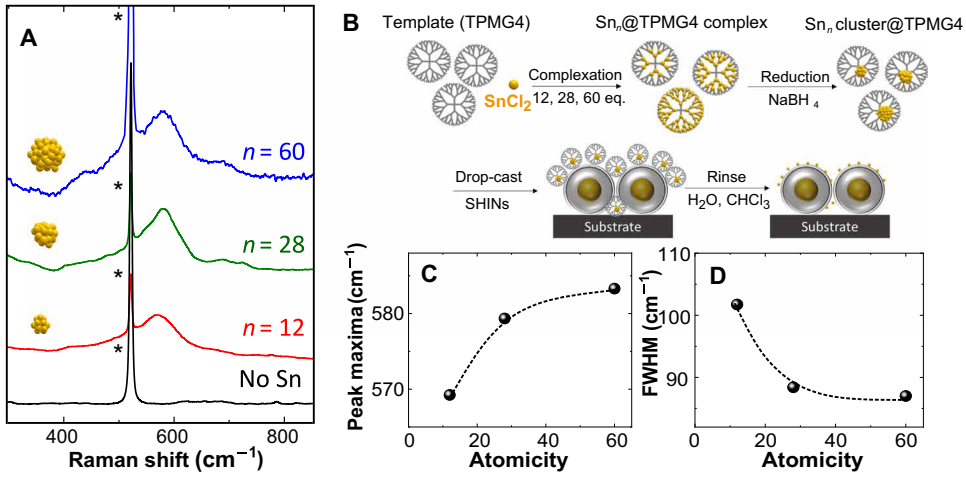

Fig. 3. Direct spectroscopic observations of Sn oxide SNCs on Au@Ag SHINs. (**A**) SHINER spectra of Sn oxide SNCs deposited on Au@Ag SHINs on Si substrates, compared with a reference spectrum obtained without $SnCl_2$ as a blank. A sharp signal from the silicon substrate is indicated by an asterisk. (**B**) A schematic diagram of the process used to prepare samples for SHINERS analysis of Sn oxide SNCs. Effects of atomicity on (**C**) the peak position and (**D**) FWHM values.

in this work is rather "raw (not completely oxidized)." Subsequently, Sn oxide SNCs were loaded on the Au@Ag SHINs coated on Si substrates to allow high-sensitivity Raman spectroscopic characterization (Fig. 1). Energy-dispersive x-ray spectroscopy (EDS) and elemental mapping analyses confirmed the presence of homogeneously distributed Sn on the Au@Ag SHIN surfaces (fig. S6).

The bulk SnO_2 crystals show three Raman bands at 476, 635, and 776 cm^{-1} in a normal Raman spectrum, characteristic of a rutile-type Sn oxide structure (fig. S7), which were assigned to the E_g, A_{1g}, and B_{2g} vibration modes, respectively (*25*). In contrast, the SHINER spectra of the Sn oxide SNCs contained only a single intense but broad peak, with a maximum between 569 and 583 cm^{-1} (Fig. 3A). This peak cannot be ascribed to any of the modes predicted by group theory. Sn oxide nanoparticles with sizes of 2 to 5 nm have been reported to exhibit unique vibrations in the range of 500 to 600 cm^{-1}, accompanied by a sharp A_{1g} signal (*26*–*32*). In these literature, the broad peak was attributed to grain size, surface disorder, or amorphous structure effects, based on phenomenological considerations. Note that Ristić *et al.* (*33*) ascribed a broad Raman band at 571 cm^{-1} to amorphous Sn^{4+} hydrous oxide. However, a detailed assignment of these intrinsic vibrational characteristics has not yet been reported because of a lack of understanding of the vibrational assignments and structural details of nanoscale Sn oxides.

The goal of the present work was to explore the nature of SNCs by assessing the structural and chemical properties of Sn oxide SNCs in detail. Note that the intense A_{1g} peak generated by bulk SnO_2 disappears completely in the spectra produced by SNCs (Fig. 3A). In addition, the emergence of a broad signal is typically indicative of the accumulation of signals from Sn—O bonds with slightly different binding configurations. Thus, the loss of the A_{1g} peak and the appearance of the broad signal suggest the complete deformation of the crystalline structure of rutile type Sn oxide in the SNCs, along with the formation of multiatom clusters with distorted atomic configurations.

The positions of the Raman peak maxima and the full width at half maximum (FWHM) values of the undefined peaks are plotted as functions of the constituent atomicity in Fig. 3, C and D, respectively. A red shift and broadening of the peak with decreasing SNC size are apparent, indicating that the cluster size, even at the subnanoscale, affects the spectral properties sensitively.

Structure simulations and vibration analyses of Sn oxide SNCs

Further structural deliberation of the Sn oxide SNCs required ab initio theoretical calculations that simulated the vibrational features in Raman spectra based on the atomic configurations of model clusters. For this purpose, density functional theory (DFT) calculations (*34*) were performed, using model Sn oxide SNCs with stoichiometric compositions estimated from XPS data (fig. S5D). These models were constructed starting from a rutile-type crystal structure, which was subsequently geometrically optimized to obtain a minimum energy configuration. Vibrational spectra were then simulated based on the structures obtained for each model SNCs and compared to the experimental SHINER spectra (Fig. 4). The simulated Raman spectrum for $Sn_{12}O_{17}$ contained multiple signals over a wide range of wavelengths, including a broad peak in the range of 500 to 800 cm^{-1} (Fig. 4A, dashed line), which is 100 cm^{-1} higher than that observed in the actual SHINER spectra (Fig. 4A, solid line). This clear discrepancy between experimental and theoretical spectra required a reconsideration of the model structure for the vibrational simulations. A survey scan over wide energy range during XPS analyses of each Sn oxide SNC identified the presence of Ag, Au, Sn, O, and Si from either the Au@Ag SHINs or Sn oxide SNCs, while no other elements were detected. Therefore, the reconsideration of the model did not involve other elements, unless those were undetectable by XPS, such as H and He. As Ristić *et al.* (*33*) indicated that the broad Raman band can be ascribed to amorphous Sn hydrous oxide, it is reasonable to include hydroxyl groups in the model, originated from the $NaBH_4$ methanol solution, atmospheric water vapor, or the silica shells of the Au@Ag SHINs adjacent to the Sn oxide SNCs.

To assess the effects of hydroxyl groups without changing the oxidation state of Sn as determined from the XPS data, we added water molecules to the stoichiometric $Sn_{12}O_{17}$ formula one by one while simulating the resulting Raman spectra (fig. S8, A to E). Structure optimization simulations demonstrated that all hydroxyl groups protruded outward from the surface of the model SNC structures, sporadically forming hydrogen bonds with neighboring atoms in Sn—O—Sn configurations (Fig. 4C and fig. S8, F to I). As the water content was increased from $Sn_{12}O_{17}$ to $Sn_{12}O_{25}H_{16}$, the peak position of the main broad Raman band gradually shifted to the lower wave number region from 634 to 571 cm^{-1} (fig. S8J). Among these simulated Raman spectra, the $Sn_{12}O_{25}H_{16}$ spectrum showed a maximum at 571 cm^{-1} (Fig. 4B, dashed line), and the spectral shape was surprisingly similar to that of the experimental spectrum acquired from the Sn_{12} oxide SNCs (Fig. 4B, solid line). Similar simulation processes were implemented for Sn_{28} and Sn_{60} SNCs, and both $Sn_{28}O_{48}H_{12}$ and $Sn_{60}O_{112}H_{24}$ were found to produce broad bands at similar frequencies to those observed in the corresponding SHINER spectra (fig. S9). The broad bands in the SHINER spectra were also blue-shifted by 10 to 30 cm^{-1} when Sn oxide SNCs were calcined at 300°C (fig. S9), suggesting that water was removed, leading to a partial decrease in surface hydroxyl groups. As a consequence, the broad band was shifted to a higher wave number region, as predicted by the theoretical vibration analyses with different amounts of H_2O addition. The variations in the main peak position upon calcination therefore provide evidence for the presence of hydroxyl group in the SNCs.

As listed in fig. S9D, hydrated species are all thermodynamically more stable than unhydrated species. This is similar to the fact that metal oxides such as silica generally have a number of hydroxyl terminals on their surfaces. On the other hand, quantitative discussion on the amount of hydration is difficult, because it is indispensable for this discussion to take into consideration the condensed phase of water surrounding Sn oxide SNCs as well as a number of isomeric structures of SNCs and conformational patterns of hydration. In the present study, the amount of hydration was practically determined such that the simulated Raman spectra reproduce the experimental ones. The most important point is that the consideration of hydration improves the simulated Raman spectra, thereby reproducing the experimental ones very well.

The above results demonstrate that simulated spectra based on vibrational analysis accurately reproduced the spectral shapes observed in the experimental SHINERS studies. The modification of atomic coordinates, such as the introduction of O vacancies and hydroxyl species, is known to change the local morphology of SNCs, which, in turn, affects the corresponding vibrational features. Therefore, reproducing unique experimental Raman spectra by simulated vibrational analyses can corroborate these morphological parameters, providing further information regarding the structure-chemical activity correlation of Sn oxide SNCs during the CO oxidation reaction (*17*).

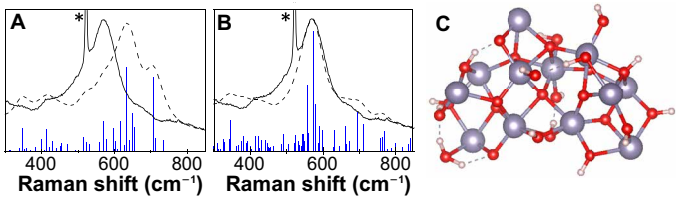

Fig. 4. Structure simulations and vibration analyses of Sn_{12} oxide SNCs. Simulated spectra (dashed line) of (**A**) $Sn_{12}O_{17}$ and (**B**) $Sn_{12}O_{25}H_{16}$ along with the spectrum of Sn_{12} oxide SNCs acquired using the Au@Ag SHINERS method (solid line). (**C**) $Sn_{12}O_{25}H_{16}$ cluster structure as simulated by DFT calculations after the structural optimization process. The Raman signal from the silicon substrate is indicated by an asterisk.

DISCUSSION

On the basis of the vibrational analyses of model SNCs in this study, hydroxyl groups appear to be responsible for the broad band around 580 to 590 cm^{-1}, as demonstrated by the agreement between the simulated and experimental SHINER spectra for Sn oxide SNCs. The stoichiometric formulae for the Sn oxide SNCs obtained from the simulations were $Sn_{60}O_{112}H_{24}$, $Sn_{28}O_{48}H_{12}$, and $Sn_{12}O_{25}H_{16}$. A closer look at the optimized chemical structures of the model Sn oxide SNCs reveals unique characteristics resulting from the structural distortion relative to the structure of bulk crystals. A statistical analysis of all the Sn—O bond length in the simulated SNC structures exhibits that the average bond length and the FWHM of the length distribution curve both increase with decreasing atomicity (fig. S10, A to D), in the same manner as the FWHM values of the broad peaks in the SHINER spectra increase (Fig. 3D). Deviations from the bulk structure were more pronounced in the case of smaller SNCs, indicating

that the Sn_{12} SNCs had a highly distorted atomic configuration with longer Sn—O bonds on average. Here, it is important to point out that the peak maxima in the SHINER spectra were red-shifted with decreases in Sn atomicity. This red shift indicates that the Sn—O bond strength in the SNCs decreases with decreasing atomicity, which is consistent with the data showing elongation of the Sn—O bonds with decreasing atomicity (fig. S10). During CO oxidation, Sn oxide catalysts work as oxygen donors, and so, it is likely that a lower Sn—O bond strength will promote bond cleavage to provide more oxygen species to enhance the CO oxidation process. In addition, it is interesting to observe that all the Sn—O bonds longer than 2.2 Å are located at the edges of the clusters, which represent the active sites for CO oxidation, and the content of surface hydroxyl groups was increased from Sn_{60} to Sn_{12} (fig. S10E). Therefore, Sn oxide SNCs with 12 Sn atoms were found to have higher hydroxyl group coverage ratio together with lower bond strengths, as demonstrated via complementary approaches with the experimental SHINERS data and theoretical simulations. These results explain well the unusual catalytic activities of smaller SNCs during the CO oxidation reaction.

Subnanosensitive spectroscopic methods elaborated in this study demonstrate its applicability to detect subnanomaterials with extremely small surface concentration. However, it is still conditional with the current method that SNCs get into the focus of the hotspots to give Raman signals in the Raman spectra. The probability of the measurements can be improved by further spatial design of the hotspots with tuning of the shape and the size of amplifiers. For instance, the introduction of star-shaped amplifiers may increase the density of hotspots on the surface, improving the probability of the measurements.

It is important to emphasize the potential impact of the current work on both the development of analytical methodology and future explorations in the field of subnanoscience. The subnanosensitive Raman spectroscopic method demonstrated in this study allows the direct detection of the spectral features of subnanoscale materials even at extremely low surface loadings. Direct detections of these small substances induce a breakthrough of further precise technological developments at the atomic level in analytical chemistry. In addition, a combined study with direct spectral observations and theoretical simulations allows the first ever rational assignment of the broad peaks in the spectra of these materials and, furthermore, reveals direct evidences to indicate the role of surface hydroxyl groups to express unique catalytic activity of Sn oxide SNCs. Detailed understanding of physical and chemical nature of substances facilitates the rational design of subnanomaterials on the atomic scale for practical applications. As a consequence, the development of subnanosensitive vibration spectroscopy will accelerate material innovation and development studies of subnanomaterials, promoting subnanoscience as an interdisciplinary research field.

MATERIALS AND METHODS

Synthesis of shell-isolated Au@Ag NPs

The Au core nanoparticles (45 nm diameter) were prepared by the citrate reduction process, following Frens method (*20*). Briefly, 100 ml of 0.01 wt % $HAuCl_4$ aqueous solution in a 300-ml round-bottom flask was first heated to boiling, and then, 0.7 ml of 1 wt % Na_3 citrate aqueous solution was quickly added. The boiling solution turned its color from pale yellow to faintly blue within 30 s and then suddenly changes into burgundy after approximately 2 min of vigorous stirring. Boiling was continued for 40 min to complete reaction and then allowed to cool down to room temperature.

Subsequently, these Au core nanoparticles were covered with silver shells of about 30 nm thick by ascorbic acid reduction process, following Uzayisenga's method (*21*). In a 100-ml conical flask, 3.09 ml of as-prepared Au core solution, 1.5 ml of 1 wt % Na_3-citrate solution, and 4.5 ml of 10 mM ascorbic acid solution were mixed at room temperature for 5 min before 0.35 ml of 20 mM $AgNO_3$ aqueous solution was slowly added dropwise at room temperature. Mixed solution was continuously stirred vigorously for 25 min to complete reaction to form Au@Ag NPs.

These Au@Ag NPs were then thoroughly covered with a pinhole-free silica shells with thicknesses in the range of 2 to 4 nm by the hydroxylation using sodium silicate (*22*). Nine milliliters of as-prepared Au@Ag NP solution, placed into a 100-ml round-bottom flask, was added to 18 ml of Milli-Q water and 0.13 ml of 1 mM APTES aqueous solution and then stirred for 15 min at room temperature. The pH of the mixture solution was adjusted to <5 by adding diluted sulfuric acid solution before adding APTES. Then, 1.07 ml of 0.54 wt % sodium silicate solution was added, followed by a 0.5 M NaOH solution to adjust the solution pH > 11.5. Then, the mixture solution was kept stirring at room temperature for a while, where the shell thickness was controlled by the reaction time. Consequent silica-shelled Au@Ag nanoparticle (Au@Ag SHIN) solution was subjected to centrifugation at 5500 rpm for 15 min, where the supernatant was removed afterward. The concentrated Au@Ag SHIN pellet at the bottom of the microtubes was diluted with Milli-Q water and centrifuged again. This procedure was repeated several times for a cleaning purpose. When APTMS (3-aminopropyltrimethoxysilane) was first used instead of APTES, as suggested in the original SHINERS methods for Au SHINs (*18*), the consequent scanning electron microscopy (SEM) images of Au@Ag SHINs revealed severe leakage of Ag, forming many Ag nanoparticles at a size of ca. 10 nm in diameter on the surface of Au@Ag SHINs, highly possible to interfere with sample SNCs. Therefore, it was replaced by APTES, where no Ag leakage was observed.

Synthesis of Sn oxide SNCs using dendrimer template method

Sn oxide SNCs Sn_{12}, Sn_{28}, and Sn_{60} were prepared by following the template methods developed in our group (*3*). Briefly, Sn-dendrimer (DPA-TPM-G4) complex was prepared by the addition of 12, 28, and 60 equivalents of $SnCl_2$ acetonitrile solution (6.3 mM) into a 1 ml of 3 μM DPA-TPM-G4 (*23*, *24*) dichloromethane solution. The complexation process was monitored by the spectral variation based on the coordination of tin chloride with the imine nitrogen atoms in titration ultraviolet-visible spectra (fig. S3). In this procedure, the yellowish DPA-TPM-G4 solution turned into orange solution. The mixture was stirred for a few minutes before a 1 ml of 238 mM $NaBH_4$ methanol solution was added for the reduction of tin chloride to metallic tin within the dendritic molecular capsule, which was gradually oxidized to tin oxide by air.

Sample preparation for advanced Raman measurements

Si substrate was first cleaned by immersing in the piranha solution (H_2SO_4:H_2O_2 = 4:1), followed by extensive rinsing with Milli-Q water. As-prepared Au@Ag SHINs solution was added by a dilute H_2SO_4 solution to lower the pH around 3, casted on the cleaned Si substrates, and subsequently dried in air. Sn oxide SNC solution was then casted

on the Au@Ag SHIN–modified Si substrate and dried in the Ar stream, followed by several extensive rinsing with Milli-Q water and chloroform. The former process was to remove inorganic substances, such as NaCl and $B(OH)_3$ generated from a sodium borohydride reduction process, while the latter process was to remove organic substances such as dendrimer molecules from the interface between SHINs and substrate before each SHINER measurement.

DFT calculations for structural and vibrational simulations

DFT calculations, for structural deliberation of Sn oxide SNCs to simulate vibrational features in Raman spectra, were performed with the BLYP functional and the LanL2DZ basis set for Sn as well as the 3-21G basis sets for H and O. Model clusters with stoichiometric compositions estimated from XPS data were first constructed by capturing from a rutile-type crystal structure. Later, water molecules were further added to the stoichiometric formula of each SNC. The constructed model clusters were geometrically optimized, with which the vibrational analyses were performed. On the basis of the vibrational analyses, Raman scattering intensities for various resonance peaks were calculated (blue solid lines), and subsequently, Raman spectra were simulated by adding a line width to each scattering intensity (black dashed curves). The line width was given by a Gaussian function with a half width of 30 cm^{-1}. In addition, it should also be noted that a vibrational analysis usually gives a slight difference between the calculated vibrational frequencies and experimental ones due to insufficient description of anharmonicity. It is, however, well known that this inaccuracy can be resolved by scaling the calculated frequencies (*35*). In the present study, a scaling factor 0.952 was used, which was determined such that an experimental Raman spectrum of a rutile-type Sn oxide crystal was reproduced in a first-principles manner. For the crystal, periodic boundary condition DFT calculations were carried out at the same level of theory as above. All the DFT calculations were conducted with the Gaussian 16, Rev. B.01 program package (*34*).

Theoretical simulation of electromagnetic enhancement fields at the gap between two Ag nanoparticles

The strength of the electromagnetic fields generated by the localized surface plasmon resonance at the vicinity of Ag nanoparticles strongly depends on the size of the Ag nanoparticles, which can be estimated using the 3D-FDTD simulation method. The commercial software FDTD Solutions (Lumerical Company) and KeyFDTD (Science and Technology Institute) were used to simulate the electromagnetic field and enhancement factors of Ag spherical nanoparticles in the function of diameter of Ag nanoparticles in the presence and absence of Au core particles (*19*).

The objective model consisted of two Ag-SiO_2 core-shell nanoparticles placed on a Si substrate, without a gap between them. The diameter of Ag nanoparticles was varied in the range from 70 to 140 nm, while the SiO_2 shell thickness was adjusted to 2 nm, practically providing 4-nm gap between two nanoparticles. The optical influence from Au core nanoparticle in the electric field distribution around Au@Ag SHINs was evaluated by varying Au core size from 0 to 100 nm, while the size of Ag outer sphere and the gap between two particles were fixed at 100 and 4 nm, respectively.

A linearly polarized plane wave with a wavelength of 532 nm was incident perpendicularly to the substrate from the top of the particles. A rough mesh covered all the simulated area, while fine meshes (a grid of 1 nm) were set around the center of dimers, as well as at gaps between substrate and nanoparticle. The electric field distribution was recorded as a plane perpendicular to the substrate and containing the centers of the two nanoparticles.

SUPPLEMENTARY MATERIALS

Supplementary material for this article is available at http://advances.sciencemag.org/cgi/content/full/5/12/eaax6455/DC1

Supplementary Materials and Methods

Fig. S1. Characterization of the Au seed and Au@Ag NPs.

Fig. S2. Formation of silica shell on Au@Ag amplifiers and the thickness effect on the Raman enhancement.

Fig. S3. Ultraviolet-visible spectral monitoring of the metal complex accumulation process.

Fig. S4. Structural characterization of Sn oxide SNCs by HAADF-STEM and AFM.

Fig. S5. Oxidation states of Sn oxide SNCs.

Fig. S6. Attachment of Sn oxide SNCs on Au@Ag SHINs.

Fig. S7. A normal Raman spectrum of bulk Sn oxide crystals.

Fig. S8. Vibration analyses of Sn_{12} oxide SNCs with the addition of water.

Fig. S9. Effect of H_2O addition on simulated and SHINER spectra.

Fig. S10. Statistic distribution of Sn—O bonds in Sn oxide SNCs.

References (*36*, *37*)

REFERENCES AND NOTES

1. Y. Lu, W. Chen, Sub-nanometre sized metal clusters: From synthetic challenges to the unique property discoveries. *Chem. Soc. Rev.* **41**, 3594–3623 (2012).
2. K. Yamamoto, M. Higuchi, S. Shiki, M. Tsuruta, H. Chiba, Stepwise radial complexation of imine group in phenylazomethine dendrimers. *Nature* **415**, 509–511 (2002).
3. K. Yamamoto, T. Imaoka, Precision synthesis of subnanoparticles using dendrimers as a superatom synthesizer. *Acc. Chem. Res.* **47**, 1127–1136 (2014).
4. T. Tsukamoto, T. Kambe, A. Nakao, T. Imaoka, K. Yamamoto, Atom-hybridization for synthesis of polymetallic clusters. *Nat. Commun.* **9**, 3873 (2018).
5. K. Yamamoto, T. Imaoka, W. J. Chun, O. Enoki, H. Katoh, M. Takenaga, A. Sonoi, Size-specific catalytic activity of platinum clusters enhances oxygen reduction reactions. *Nat. Chem.* **1**, 397–402 (2009).
6. T. Imaoka, H. Kitazawa, W. J. Chun, K. Yamamoto, Finding the most catalytically active platinum clusters with low atomicity. *Angew. Chem. Int. Ed.* **54**, 9810–9815 (2015).
7. M. Nesselberger, M. Roefzaad, R. F. Hamou, P. U. Biedermann, F. F. Schweinberger, S. Kunz, K. Schloegl, G. K. H. Wiberg, S. Ashton, U. Heiz, K. J. J. Mayrhofer, M. Arenz, The effect of particle proximity on the oxygen reduction rate of size-selected platinum clusters. *Nat. Mater.* **12**, 919–924 (2013).
8. P. Bothra, M. Pandey, S. K. Pati, Size-selective electrocatalytic activity of $(Pt)_n/MoS_2$ for oxygen reduction reaction. *Cat. Sci. Technol.* **6**, 6389–6395 (2016).
9. S. Vajda, M. J. Pellin, J. P. Greeley, C. L. Marshall, L. A. Curtiss, G. A. Ballentine, J. W. Elam, S. Catillon-Mucherie, P. C. Redfern, F. Mehmood, P. Zapol, Subnanometre platinum clusters as highly active and selective catalysts for the oxidative dehydrogenation of propane. *Nat. Mater.* **8**, 213–216 (2009).
10. M. Takahashi, H. Koizumi, W. J. Chun, M. Kori, T. Imaoka, K. Yamamoto, Finely controlled multimetallic nanocluster catalysts for solvent-free aerobic oxidation of hydrocarbons. *Sci. Adv.* **3**, e1700101 (2017).
11. M. Huda, K. Minamisawa, T. Tsukamoto, M. Tanabe, K. Yamamoto, Aerobic toluene oxidation catalyzed by subnano metal particles. *Angew. Chem. Int. Ed.* **58**, 1002–1006 (2019).
12. N. Satoh, T. Nakashima, K. Kamikura, K. Yamamoto, Quantum size effect in TiO_2 nanoparticles prepared by finely controlled metal assembly on dendrimer templates. *Nat. Nanotechnol.* **3**, 106–111 (2008).
13. T. Imaoka, Y. Akanuma, N. Haruta, S. Tsuchiya, K. Ishihara, T. Okayasu, W. J. Chun, M. Takahashi, K. Yamamoto, Platinum clusters with precise numbers of atoms for preparative-scale catalysis. *Nat. Commun.* **8**, 688 (2017).
14. M. Batzill, U. Diebold, The surface and materials science of tin oxide. *Prog. Surf. Sci.* **79**, 47–154 (2005).
15. S. Das, V. Jayaraman, SnO2 a comprehensive review on structurers and gas sensors. *Prog. Mater. Sci.* **66**, 112–255 (2014).
16. D. Mohanta, M. Ahmaruzzaman, Tin oxide nanostructured materials: An overview of recent developments in synthesis, modifications and potential applications. *RSC Adv.* **112**, 110996–111015 (2016).
17. Y. Inomata, K. Albrecht, K. Yamamoto, Size-dependent oxidation state and CO oxidation activity of tin oxide clusters. *ACS Catal.* **8**, 451–456 (2018).
18. J. F. Li, Y. F. Huang, Y. Ding, Z. L. Yang, S. B. Li, X. S. Zhou, F. R. Fan, W. Zhang, Z. Y. Zhou, D. Y. Wu, B. Ren, Z. L. Wang, Z. Q. Tian, Shell-isolated nanoparticle-enhanced Raman spectroscopy. *Nature* **464**, 392–395 (2010).
19. T. Wang, Z. Zhang, F. Liao, Q. Cai, Y. Li, S.-T. Lee, M. Shao, The effect of dielectric constants on noble metal/semiconductor SERS enhancement: FDTD simulation and experiment validation of Ag/Ge and Ag/Si substrates. *Sci. Rep.* **4**, 4052 (2014).

20. G. Frens, Controlled nucleation for the regulation of the particle size in monodisperse gold suspensions. *Nature* **241**, 20–22 (1973).
21. V. Uzayisenga, X. D. Lin, L. M. Li, J. R. Anema, Z. L. Yang, Y. F. Huang, H. X. Lin, S. B. Li, J. F. Li, Z. Q. Tian, Synthesis, characterization and 3D-FDTD simulation of Ag@SiO_2 nanoparticles for shell-isolated nanoparticle-enhanced Raman spectroscopy. *Langmuir* **28**, 9140–9146 (2012).
22. L. M. Liz-Marzàn, M. Giersig, P. Mulvaney, Synthesis of nanosized gold-silica core-shell particles. *Langmuir* **12**, 4329–4335 (1996).
23. A. Kimoto, K. Masachika, J. S. Cho, M. Higuchi, K. Yamamoto, Novel poly(*p*-phenylenevinylene)s with a phenylazomethine dendron as a metal-collecting site. *Org. Lett.* **6**, 1179–1182 (2004).
24. O. Enoki, H. Katoh, K. Yamamoto, Synthesis and properties of a novel phenylazomethine dendrimer with a tetraphenylmethane core. *Org. Lett.* **8**, 569–571 (2006).
25. J. F. Scott, Raman spectrum of SnO_2. *J. Chem. Phys.* **53**, 852–853 (1970).
26. M. Ocaña, C. J. Serna, J. V. Gracía-Ramos, E. Matijević, A vibrational study of uniform SnO_2 powders of various morphologies. *Solid State Ion.* **63-65**, 170–177 (1993).
27. J. Zuo, C. Xu, X. Liu, C. S. Wang, C. G. Wang, Y. Hu, Y. Qian, Study of the Raman spectrum of nanometer SnO_2. *J. Appl. Phys.* **75**, 1835–1836 (1994).
28. K. N. Yu, Y. Xiong, Y. Liu, C. Xiong, Microstructural change of nano-SnO_2 grain assemblages with the annealing temperature. *Phys. Rev. B* **55**, 2666–2671 (1997).
29. L. Abello, B. Bochu, A. Gaskov, S. Koudryavtseva, G. Lucazeau, M. Roumyantseva, Structural characterization of nanocrystalline SnO_2 by x-ray and Raman spectroscopy. *J. Solid State Chem.* **135**, 78–85 (1998).
30. A. Diéguez, A. Romano-Rodríguez, A. Vilà, J. R. Morante, The complete Raman spectrum of nanometric SnO_2 particles. *J. Appl. Phys.* **90**, 1550–1557 (2001).
31. M. N. Rumyantseva, A. M. Gaskov, N. Rosman, T. Pagnier, J. R. Morante, Raman surface vibration modes in nanocrystalline SnO_2: Correlation with gas sensor performances. *Chem. Mater.* **17**, 893–901 (2005).
32. K. Vijayarangamuthu, S. Rath, Nanoparticle size, oxidation state, and sensing response of tin oxide nanopowders using Raman spectroscopy. *J. Alloys Compd.* **610**, 706–712 (2014).
33. M. Ristić, M. Ivanda, S. Popović, S. Musicć, Dependence of nanocrystalline SnO_2 particle size on synthesis route. *J. Non-Cryst. Solids* **303**, 270–280 (2002).
34. M. J. Frisch, G. W. Trucks, H. B. Schlegel, G. E. Scuseria, M. A. Robb, J. R. Cheeseman, G. Scalmani, V. Barone, G. A. Petersson, H. Nakatsuji, X. Li, M. Caricato, A. V. Marenich, J. Bloino, B. G. Janesko, R. Gomperts, B. Mennucci, H. P. Hratchian, J. V. Ortiz, A. F. Izmaylov, J. L. Sonnenberg, D. Williams-Young, F. Ding, F. Lipparini, F. Egidi, J. Goings, B. Peng, A. Petrone, T. Henderson, D. Ranasinghe, V. G. Zakrzewski, J. Gao, N. Rega, G. Zheng, W. Liang, M. Hada, M. Ehara, K. Toyota, R. Fukuda, J. Hasegawa, M. Ishida, T. Nakajima, Y. Honda, O. Kitao, H. Nakai, T. Vreven, K. Throssell, J. A. Montgomery Jr., J. E. Peralta, F. Ogliaro, M. J. Bearpark, J. J. Heyd, E. N. Brothers, K. N. Kudin, V. N. Staroverov, T. A. Keith, R. Kobayashi, J. Normand, K. Raghavachari, A. P. Rendell, J. C. Burant, S. S. Iyengar, J. Tomasi, M. Cossi, J. M. Millam, M. Klene, C. Adamo, R. Cammi, J. W. Ochterski, R. L. Martin, K. Morokuma, O. Farkas, J. B. Foresman, D. J. Fox, *Gaussian 16 Revision B.01* (Gaussian Inc., 2016).
35. A. P. Scott, L. Radom, Harmonic vibrational frequencies: An evaluation of Hartree–Fock, Møller–Plesset, quadratic configuration interaction, density functional theory, and semiempirical scale factors. *J. Phys. Chem.* **100**, 16502–16513 (1996).
36. A. K. Sinha, P. K. Manna, M. Pradhan, C. Mondal, S. M. Yusuf, T. Pal, Tin oxide with a p-n heterojunction ensures both UV and visible light photocatalytic activity. *RSC Adv.* **4**, 208–211 (2014).
37. K. G. Godinho, A. Walsh, G. W. Watson, Energetic and electronic structure analysis of intrinsic defects in SnO. *J. Phys. Chem. C* **113**, 439–448 (2009).

Acknowledgments: We thank Y. Inomata for discussions. **Funding:** This work was supported by JST ERATO (grant number JPMJER1503) and JSPS KAKENHI Grant-in-Aid for Scientific Research (S) (grant number 15H05757). A.K. acknowledges the financial support from JSPS KAKENHI Grant-in-Aid for Scientific Research (C) (grant number 17 K05896). **Author contributions:** A.K. and K.Y. conceived and designed experiments. A.K. and M.O. performed experimental works, while Y.T., Y.Y., and N.H. carried out the theoretical calculations. A.K., N.H., and K.Y. co-wrote the manuscript. **Competing interests:** The authors declare that they have no competing interests. **Data and materials availability:** All data needed to evaluate the conclusions in the paper are present in the paper and/or the Supplementary Materials. Readers can contact A.K. and K.Y. for the access of our data. Additional data related to this paper may be requested from the authors.

Submitted 10 April 2019
Accepted 24 October 2019
Published 13 December 2019
10.1126/sciadv.aax6455

Citation: A. Kuzume, M. Ozawa, Y. Tang, Y. Yamada, N. Haruta, K. Yamamoto, Ultrahigh sensitive Raman spectroscopy for subnanoscience: Direct observation of tin oxide clusters. *Sci. Adv.* **5**, eaax6455 (2019).